Profiling site-specific cell states of Ewing Sarcoma xenografts in zebrafish

Dagan Segal[1,2], Hanieh Mazloom-Farsibaf[1,2], Bo-Jui Chang[2], Philippe Roudot[1,2], Reto Fiolka[2], Mikako Warren[3], James F. Amatruda[3*] and Gaudenz Danuser[1,2*]

Abstract:

A key challenge in cancer research is to identify functional cell states as they relate to specific tissue microenvironments**.** In this work, we present a quantitative high-resolution imaging assay of cancer cell morphology in zebrafish xenografts to probe functional adaptation to variable cell extrinsic cues and molecular interventions. We focus on Ewing Sarcoma, a pediatric cancer driven by a single oncogenic fusion protein EWSR1-FLI1, and with little to no additional somatic mutations, making it a prototypical form of cancer whose adaptation is likely driven by acute, non-genomic mechanisms. By applying machine learning approaches to 3D cell shapes, we find systematic shifts in the distribution of cell morphological states between seeding sites in the fish embryo, as well as between cells with differential expression of EWSR1-FLI1 in an environmentally sensitive fashion. We propose a model where Ewing Sarcoma cancer cell plasticity is sensitive both to expression fluctuation of EWSR1-FLI1 and signals from the surrounding tissue microenvironment, with either or both factors possibly contributing to metastatic potential.

Introduction:

Metastasis is the primary cause of cancer-related deaths [1]. The ability of a metastatic cancer cell to arrive, survive and thrive in diverse tissue microenvironments (MEs) is a testament to their adaptability. Despite decades of research, our understanding of the mechanisms of metastasis has many remaining gaps, making this the single biggest obstacle to successful cancer treatment [1, 2]. Therefore, a key technical and conceptual challenge in cancer research is to identify and probe relevant functional differences between cancer cells as they relate to adaptation to specific tissue microenvironments.

Historically, cancer research has predominantly relied on the mouse for investigation of the progression of metastasis [3]. However, for the task of probing functional adaptation of cancer cells in the secondary tissue environment, this model has several limitations. Cellular responses are likely very dynamic and heterogeneous, and meaningful functional plasticity is super-imposed by random cell-to-cell variations that need to be filtered from the phenotype distributions. The mouse provides neither easy access to most metastatic sites nor the throughput necessary to fulfill this requirement. As an alternative, 2D and 3D cell culture have been exploited for studying cancer cell heterogeneity [4, 5], but for the understanding functional adaptation they lack the relevant micro-environmental complexity of an organism. Here, we propose human cancer cell xenografts in zebrafish larvae as the currently best compromise between the competing quests for environmental diversity, experimental access, and sufficient throughput to acquire meaningful descriptions of cancer cell adaptation [5-8]: (1) Zebrafish represents a living organism with various complex tissue microenvironments, with tissue mechanics, physiology, and disease susceptibility that is highly conserved with those of humans [6, 9] (2) The optical transparency of zebrafish grants easy experimental access to any metastatic site by high-resolution imaging, and (3) a single experimental session can yield hundreds of successful xenografts, allowing for high throughput within a single comparative study.

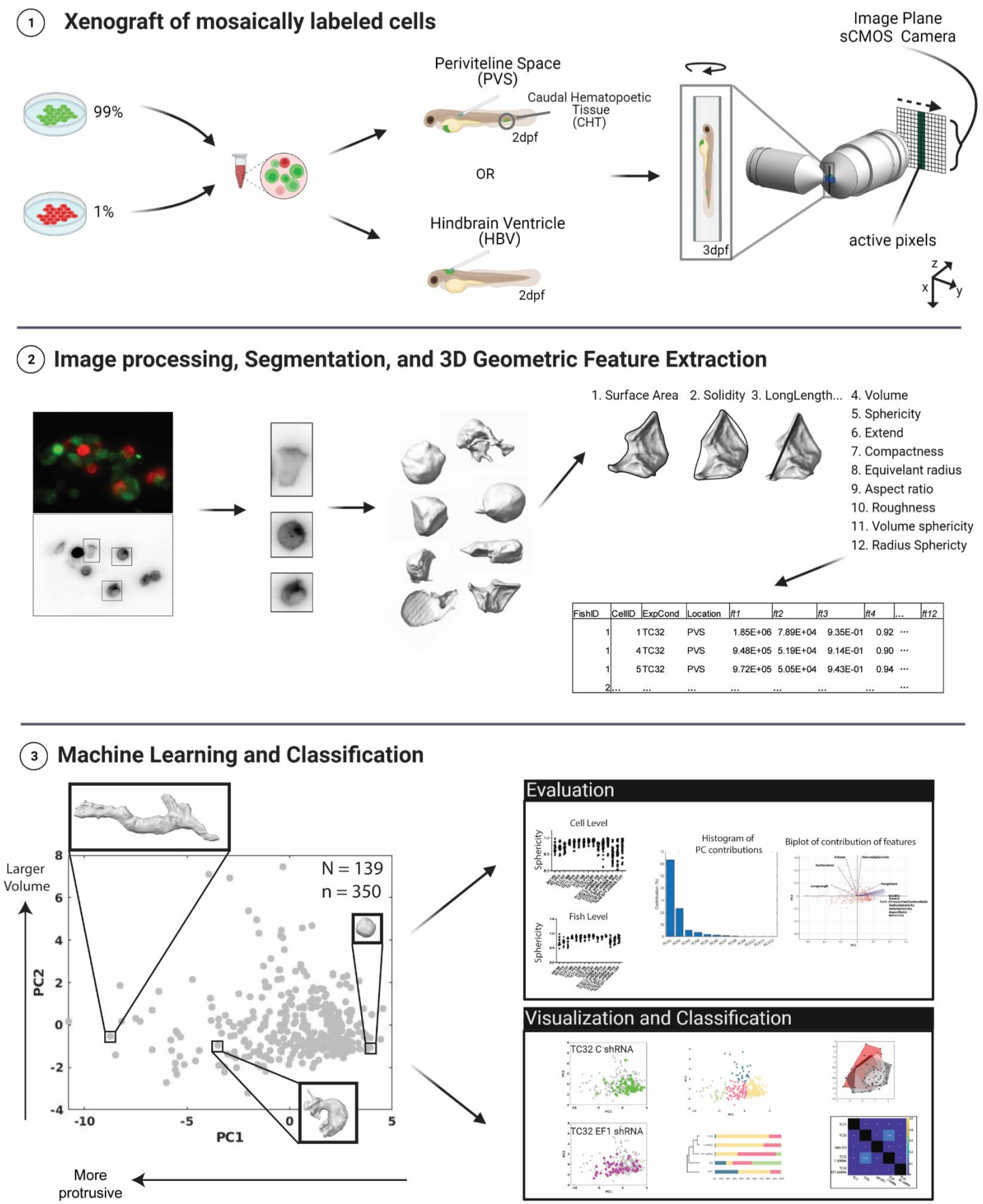
1 Xenograft of mosaically labeled cells
99%
1%
Periviteline Space (PVS)
Caudal Hematopoetic Tissue (CHT)
2dpf
OR
Hindbrain Ventricle (HBV)
2dpf
Image Plane
sCMOS Camera
3dpf
active pixels
z
x
y
2 Image processing, Segmentation, and 3D Geometric Feature Extraction
1. Surface Area
2. Solidity
3. LongLength...
4. Volume
5. Sphericity
6. Extend
7. Compactness
8. Equivelant radius
9. Aspect ratio
10. Roughness
11. Volume sphericity
12. Radius Sphericty
FishID CellID ExpCond Location ft1 ft2 ft3 ft4 ... ft12
1 1 TC32 PVS 1.85E+06 7.89E+04 9.35E-01 0.92 ...
1 4 TC32 PVS 9.48E+05 5.19E+04 9.14E-01 0.90 ...
1 5 TC32 PVS 9.72E+05 5.05E+04 9.43E-01 0.94 ...
2 ... ...
3 Machine Learning and Classification
Larger Volume
More protrusive
PC2
PC1
N = 139
n = 350
Evaluation
Cell Level
Fish Level
Sphericity
Histogram of PC contributions
Biplot of contribution of features
Visualization and Classification
TC32 C shRNA
TC32 EF1 shRNA

Figure 1: Machine Learning of cell shapes in cancer cell xenografts in zebrafish larvae. We present an experimental and analytical pipeline to identify single-cell morphologies within tissues of zebrafish larvae and identify differences in morphological cell states by geometric feature extraction, principal component analysis, and machine-learning-based classification, as follows. (1) In order to distinguish shapes of individual cells, we prepared a mosaic cell mixture consisting of 90-99% of cells labeled with a green-emitting fluorophore and 1-10% of cells labeled with a red-emitting fluorophore, or vice versa. We then injected the cell mixture into the Perivitelline space (PVS) or Hindbrain Ventricle (HBV) of 2-day-old zebrafish larvae. For PVS injections, we selected specifically for injected larvae which also have xenografted cells in the caudal hematopoietic tissue (CHT) immediately following injection. Fish larvae were fixed at 3 days post fertilization (dpf) and imaged using an Axially Swept Light Sheet Microscope (ASLM), which is optimized for maximum throughput, resolution, and flexibility of sample orientation. High axial resolution is obtained by combining a thin, moving light-sheet with a synchronized rolling shutter (active pixels) that blocks out of focus fluorescence on the image plane on an sCMOS Camera. (2) Individual cells were computationally extracted from mosaically labeled image data which after image processing are segmented into 3D volumes. We then measured 12 global 3D geometric features as listed, and each cell was indexed according to fish, location, and cell type. (3) Using Principal Component Analysis (PCA) we captured the heterogeneity of morphological cell states. PC1 captured the protrusive state of the cell, while PC2 was influenced largely by volume (insets). We evaluated our analytical pipeline and used several visualization and classification techniques to capture differences among heterogeneous single-cell data.

This work sets the stage for development of human cancer xenografts in zebrafish as a model for unraveling mechanisms of cell adaptation during metastasis. As an initial readout of plastic cell behaviors, we focus on cell morphological variation. Cell morphology is the integrated response of cells to autonomous cues [10-15], mechanical and chemical interactions with the microenvironment [16-18], as well as a functional proxy for proliferation [19] [20] and cell death [21, 22]. Accordingly, pathologists have relied for decades on morphological patterns to stratify cancer disease states and to deliver specific diagnoses that guide treatment. With the recent development of machine learning, cell morphology is emerging as an increasingly quantitative correlate to particular molecular cell states [12, 23-27].

Studying cancer cell adaptation is of particular importance in pediatric cancers. While clonal heterogeneity and selection is thought to drive adaptation during metastasis of several adult cancers[28], many pediatric cancers exhibit a very low mutational burden beyond a single driving mutation [29] [30], suggesting non-genetic mechanisms may dominate the process of cell adaptation. In this work, we focus specifically on Ewing Sarcoma (EwS) as a prototype of pediatric cancers. EwS is the second most common pediatric bone tumor, characterized by a chromosomal translocation fusing members of the *FUS/EWSR1/TAF15* family to *ETS* transcription factors, the most common of which creates the *EWSR1-FLI1* (*EF1*) fusion oncogene [31, 32]. As with most other pediatric sarcomas[33], presence of metastasis is by far the most prominent adverse prognostic factor in EwS [31]. The specific tissue environment appears to play a factor in the degree of malignancy in EwS [34-37], as well as other pediatric sarcomas[38] [39]. For example, pelvic primary tumors appear to correlate with poorer prognosis and are more prone to metastasis compared to other primary sites, and patients who have metastasis only to lung have improved survival compared to those with metastasis to bone or bone marrow [34].

Thus, we assembled a quantitative high-resolution imaging assay of EwS cell morphology in xenografts to probe the morphological variation as a proxy to functional adaptation in diverse microenvironments and experimental molecular interventions. By machine learning of 3D cell shapes, we found systematic shifts in the distribution of cell morphological states between seeding sites in the fish embryo, as well as between control expression and knockdown of *EWSR1-FLI1* in an environmentally sensitive fashion.

We also found that proliferative but not apoptotic states of EwS cells differed between the tissue microenvironments. We propose a model where EwS cancer cell plasticity is sensitive both to fluctuations of EWSR1-FLI1 and signals from the surrounding tissue microenvironment, with either or both of these factors possibly contributing to metastatic potential.

Results:

Classification of morphologies captures heterogeneity of cell states in Ewing Sarcoma cells

We present an experimental and analytical pipeline to identify single-cell morphologies within tissues of zebrafish larvae and identify differences in morphological cell states (Figure 1). Using geometric feature extraction, principal component analysis, and machine-learning-based classification, we examined heterogeneity as a function of cell type, oncogene expression level, and tissue microenvironment. To distinguish single cells, mixtures of cells tagged with either a red-emitting (90-99% of cell mixture), or a green-emitting filamentous actin marker F-Tractin (1-10% of cell mixture) were injected into 2-day old zebrafish larvae. In contrast to other works that have used xenografts in zebrafish to model the early steps of metastatic dissemination [6], this framework aims to model site-specific cellular adaptation during metastatic colonization, to three specific seeding sites: the hindbrain ventricle (HBV), perivitelline space (PVS), and, by rapid passive transport during injection, the caudal hematopoietic tissue (CHT).

We obtained images of cells within the three seeding sites using an Axially Swept Light-sheet Microscope (ASLM) [40, 41]. Light-sheet Fluorescence Microscopy (LSFM), when compared to other imaging modalities [42] and combined with the high throughput of the zebrafish model [8] enabled acquisition of a dataset of sufficient size to provide quantitative analysis. ASLM provided the added advantage over standard ASLM techniques of near-isotropic axial resolution spanning larger volumes, allowing for more accurate 3D measurements. Using ASLM, we imaged 139 fish larvae (3 days post-fertilization) xenografted with fluorescently labeled cell mixtures, which enabled 3D segmentation after image processing of 350 individual cells. We then computationally extracted single cells from the images for 3D segmentation. Using the extracted 3D volumes, we measured 12 basic geometric features (Volume, Surface Area, Solidity, Sphericity, Long Length, Extend, Compactness, Equivalent radius, Aspect ratio, Roughness, Volume sphericity, Radius sphericity, Spherical radius ratio, and Circumscribed sphere area ratio (Figure 1, Table S1)). Examination of individual geometric features at the single-cell level or fish-level showed similar distributions, suggesting low fish-to-fish variability (Figure S1a).

Since individual features were not able to capture the large heterogeneity of morphological cell states observed (Figure S1b), we applied principal component analysis (PCA) based on the twelve global geometric features described (Figure 1). The first two principal components (PCs) captured 86% of the heterogeneity within the data, indicating a high-level of dimensionality reduction (Figure S1c). PC1 and PC2 together captured well the continuous states of cell morphology observed qualitatively. Specifically, PC1 captured the protrusive state of the cell, while PC2 was dominated by cell size and rectangularity. This corresponds well to the dominant features contributing to PC1 (i.e. Sphericity and Aspect Ratio) and PC2 (Volume and Surface Area, Figure S1d,e). The PCA was subsequently used as a basis for further evaluation, visualization, and classification of the data.

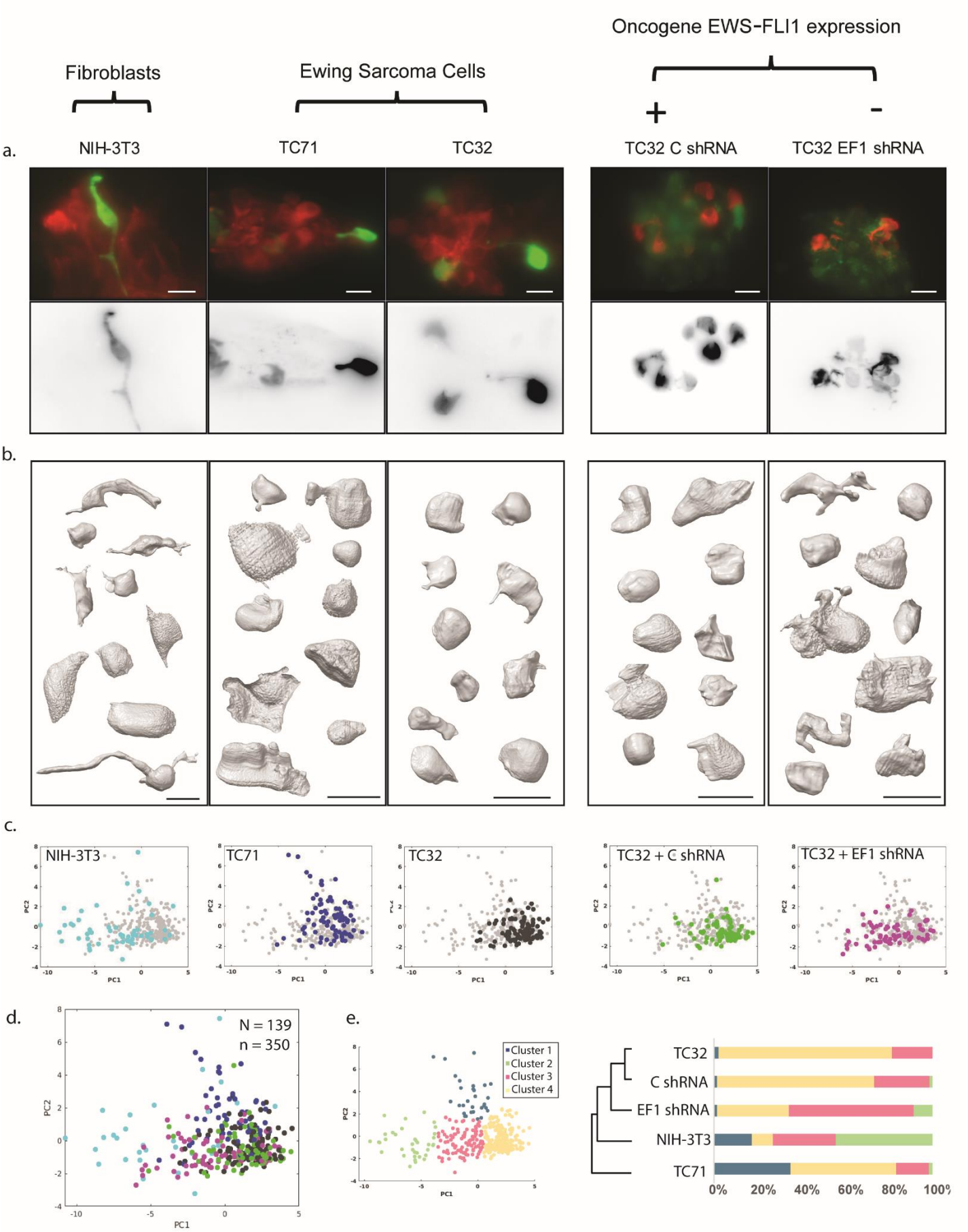
Oncogene EWS-FLI1 expression
Fibroblasts
Ewing Sarcoma Cells
+
-
a.
NIH-3T3
TC71
TC32
TC32 C shRNA
TC32 EF1 shRNA
b.
c.
NIH-3T3
TC71
TC32
TC32 + C shRNA
TC32 + EF1 shRNA
PC1
PC2
d.
N = 139
n = 350
e.
Cluster 1
Cluster 2
Cluster 3
Cluster 4
TC32
C shRNA
EF1 shRNA
NIH-3T3
TC71
0%
20%
40%
60%
80%
100%

Figure 2: Classification of morphologies captures heterogeneity of cell states in EwS cells. (a, left) EwS (a, TC32 and TC71) or fibroblast (a, NIH-3T3) cells expressing FTractin-GFP (green in upper panel, grey in lower panel) or FTractin-mRuby2 (red), in zebrafish HBV (3dpf). **(a, right)** TC32 cells expressing a doxycycline-induced cassette which includes a cytoplasmic GFP (upper panel, green) as well as (scrambled shRNA (C shRNA) or shRNA targeting EF1 (EF1 shRNA). A subset of cells also express FTractin-mRuby2 (red in upper panel, grey in lower panel), allowing for mosaic labeling of single cell morphologies. **(b)** 10 representative 3D cell renderings are displayed within each experimental group, pooled from all three tissue MEs. Note the distinction in cell shape and size particularly in NIH-3T3 (left-most panel) and TC32 EF1 shRNA (right-most panel) compared to other experimental groups. **(c-d)** PCA of all experimental groups shown individually (c) or together (d). **(e)** K-means based clustering followed by hierarchical clustering allows visualization of relationships between experimental groups. Note distinctions in all experimental groups. Scale bars

We examined single cell morphologies of two Ewing Sarcoma cell lines, TC32 and TC71, *in situ* in zebrafish larvae, and as a point of comparison, the non-transformed fibroblast cell line NIH-3T3 (Figure 2a). We also examined the role of expression levels of EF1, the driving fusion-oncogene for EwS, since previous *in vitro* works showed that knockdown of EF1 led to an EMT-like shape transition, which was coupled to reduced proliferation but no difference in cell survival [43]. To accomplish this, we injected TC32 Ewing sarcoma cells expressing a doxycycline-inducible scrambled (C shRNA) or EF1 (EF1 shRNA) targeting shRNA and cytoplasmic GFP tag and with (1-10%) or without (90-99%) ubiquitously driven F-Tractin-MRuby2. Visual inspection of 3D renderings of segmented cells already showed distinct differences between NIH-3T3 and EwS cells, and between cells with wild-type or knockdown levels of EF1 expression, pooled from all three tissue MEs (Figure 2b). PCA based on global geometric features revealed distinct distributions in PC space between experimental groups (Figure 2c,d).

Using K-means followed by hierarchical clustering and pairwise permutation tests, we observed differences between all experimental groups except for TC32 and TC32 + C shRNA, which were largely overlapping (Figure 2e, Figure S1f). NIH-3T3 were characterized by a more protrusive cell state, while TC71 resembled TC32 in protrusive state but was higher in volume. TC32 cells knocked down for EF1 expression displayed a marked shift to a more protrusive state, with sphericity comparable to that of fibroblasts (Figure S1b), and was distinct from control groups. This observation is consistent with previous works *in vitro* describing morphological shifts to a more mesenchymal state upon EF1 knock-down [43]. Of note, exclusion of NIH-3T3 as an outlier group resulted in only a minor shift in PCA space and relative contribution of features (Figure S1g-h), suggesting that the PCA of the 12 global 3D features constitutes a robust space for the definition of cell morphological classes. Overall, these results demonstrate the applicability of a universal morphology classifier in capturing cell state differences across cell types and experimental conditions, and demonstrate that oncogene levels affect EwS cell state *in vivo*.

Tissue microenvironment affects EwS cell morphologies

In order to examine whether EwS cells systematically adapt their cell state as a function of tissue ME, we first compared proliferation and cell death states between the hindbrain ventricles (HBV), the perivitelline space (PVS), and the caudal hematopoetic tissue (CHT), each representing a unique biochemical and mechanical ME (Figure 3a). For example, the HBV are cavities which contain cerebrospinal fluid, rich in hormones, proteoglycans, and ions [44-46], the PVS is a sandwiched, avascular region between two malleable membranes surrounding the yolk [47] and the CHT is a compact, thin, crowded region containing multiple cell types, including endothelial cells, stromal cell and hematopoietic cells for which it serves as a stem cell niche [48-50]. We examined cell proliferation

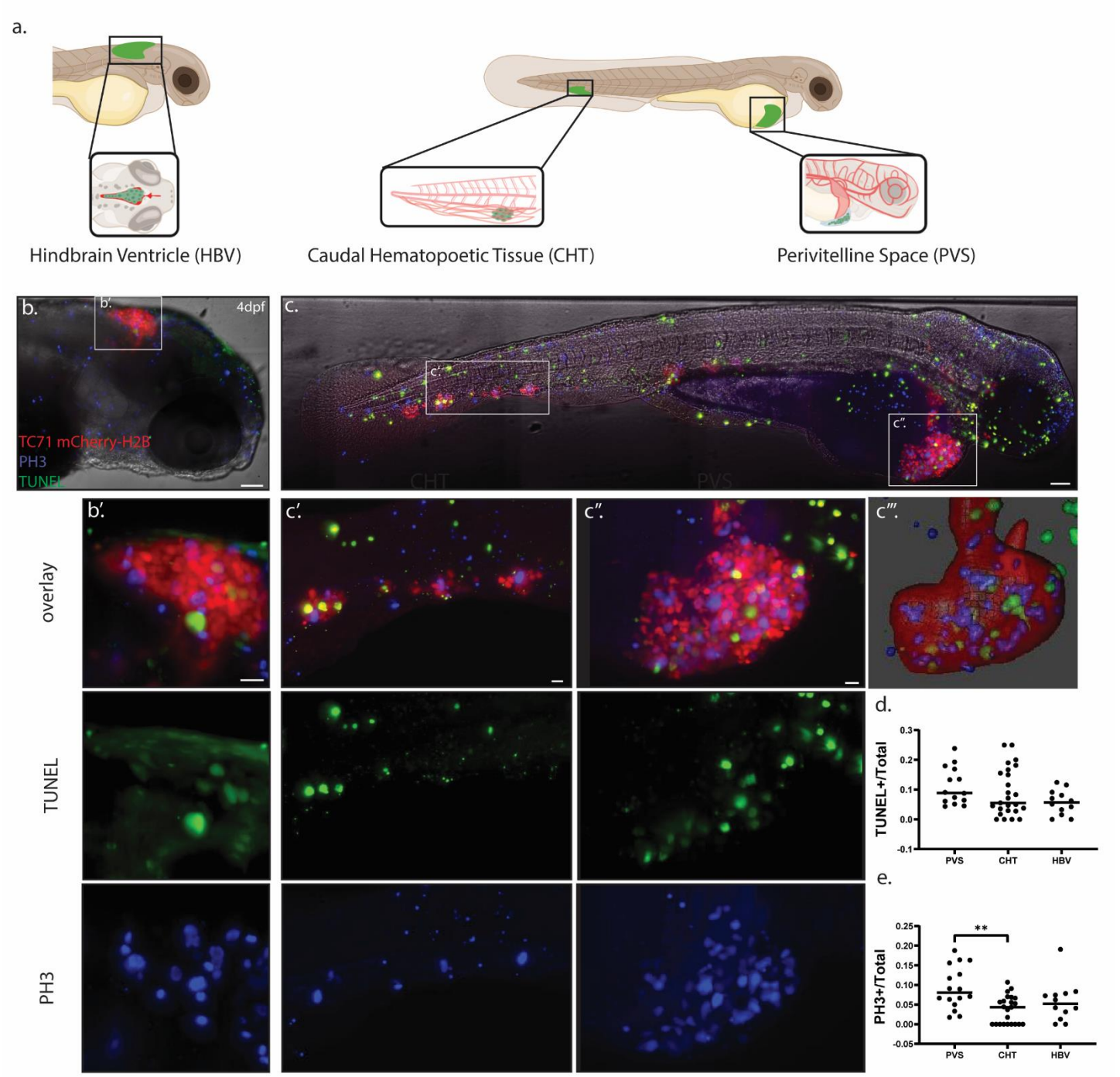

Figure 3: Proliferation but not apoptosis change as a function of tissue microenvironment. (a) Comparison of single cell morphologies were made as a function of seeding site within the zebrafish larvae, each representing a distinct tissue ME. The hindbrain ventricle (HBV) is a mostly fluid-filled compartment (a), the perivitelline space is a small, compressed region sandwiched between two membranes surrounding the yolk, and the caudal hematopoietic tissue (CHT) is a narrow region rich in vasculature. **(b-c)** TC71 cells expressing nuclear marker mCherry-H2B (red), within the HBV (inset, enlarged in b'), CHT (inset, enlarged in c'), or PVS (inset, enlarged in c''), of fish larvae (4dpf). Fish are immunostained for proliferation marker PH3 (blue) and apoptotic staining TUNEL (green). Measurements are made on 3D volumes, as rendered in c'''. **(d-e)** Apoptotic rate is similarly low across all three regions (d), while proliferation rate appears to be highest in PVS compared to other regions (e). Scale bars 100 µm (b,c) and 20 µm (b'-c, c'').

and cell death at the tissue ME level by immunostaining for proliferative marker Phospho-Histone 3 (PH3) or the apoptotic marker TUNEL (Figure 3b-c), or by measuring change in cluster size over 4 days

(S2a-c). While apoptosis was similarly low across all threetissue MEs (less than 10% on average, Figure 3d), proliferation and growth rates were higher in PVS compared to other regions (Figure 3e, Figure S2d). Note that the number of cells greatly varied between regions (Figure S2e), a difference that likely arose from differences in initial seeding rather than cell growth. However, no clear correlation was seen between proliferation rate and cluster size (Figure S2f) or fold growth and initial cluster size (Figure S2a-c), suggesting cluster size may not be a major driver of differences in cell growth.

We next applied our classification of cell morphologies as a surrogate of cell function to examine single cell state variations between distinct tissue MEs (Figure 4). Bagplots (i.e. bivariate boxplots) [51] enabled visualization of differences in distributions in PC space. Differences were further quantified by assembly of similarity matrices based on pairwise permutation tests between regions. Examination of NIH-3T3 fibroblasts revealed highly heterogeneous cell morphologies, with largely overlapping distribution in all three seeding sites, suggesting lack of sensitivity to environmental cues in these non-transformed cells (Figure 4a). In contrast, The EwS cell lines TC32 (Figure 4b) and TC71 (Figure 4c) showed some distinction in distributions of cell morphologies as a function of seeding site. For example, TC32 cells in the PVS and CHT were largely overlapping, but cells in the HBV shifted to the upper left in PC space, indicating more protrusive, larger cells. Accordingly, these cells were also lower in sphericity and higher in volume (Figure S3). TC71 cell distributions in the PVS and HBV shifted left in PCA space compared to CHT (Figure 4c), while showing no significant differences in sphericity or volume (Figure S3). Overall, the Ewing Sarcoma cells showed more tissue-specific specialization compared to the non-transformed fibroblasts.

The observation that EwS cells tend to be more protrusive in the HBV was somewhat paradoxical, given that the fluid-filled compartment is likely softer than PVS and CHT, a mechanical environment usually associated with rounded cells [18]. On the other hand, this environment may be enriched for specific chemical signaling cues which trigger neural differentiation [44, 45]. Closer examination of the architecture of this region revealed that cells within the HBV created a specific cellular organization of pseudorosette-like spheroids within the cell clusters, with cellular protrusions pointing towards a center of a sphere and cell bodies organized outwards (Figure 5a-c, Movie S1). TC71 cells expressing the nuclear fluorescent marker Cherry-H2B appeared to form pseudorosette-like circles in the HBV (Figure 5d) but not the PVS or CHT (Figure S4a). This occurred in both TC32 and TC71 but not in NIH-3T3, suggesting an environmentally-triggered cue affecting the EwS cells but not the fibroblasts. Notably, these structures are comparable to those observed in a subset of clinical EwS tumor H&E stains (for example, Figure 5e). Such structures may be akin to the pseudorosettes observed in a subset of Ewing Sarcomas previously classified as peripheral Primitive Neuroectordermal tumors (ppNETs) [52-54], named by pathologists according to their limited apparent neural differentiation [55].

Cell-cell interaction, cell-crowding, and position within a cell cluster or tissue all may affect cell function and thus the morphological state [56, 57]. We therefore tested whether morphological state of EwS cells was affected by its position within a cell cluster. We classified cluster-peripheral and cluster-interior cells by measuring the fraction of an individual cell surface that was in contact with the rest of the cluster. For example, a cell may have few or no neighbors (NN,0%-20% of cell surface in contact with the cluster), be partially embedded within a cluster (PE,21%-80%) with one portion exposed to the tissue ME, or almost fully or entirely embedded within a cluster ((E,81%-100%), Figure 5f). We compared the degree of contact of EwS cells with other cells to two dominant shape features, sphericity and volume. While no correlation could be uncoupled from tissue ME for volume (Figure 5g, Figure

S4b), the few cells that showed distinctly low sphericity were all fully embedded within the cluster, regardless of seeding site (Figure 5h, Figure S4c). Of note, the TC32 cells examined showed similar

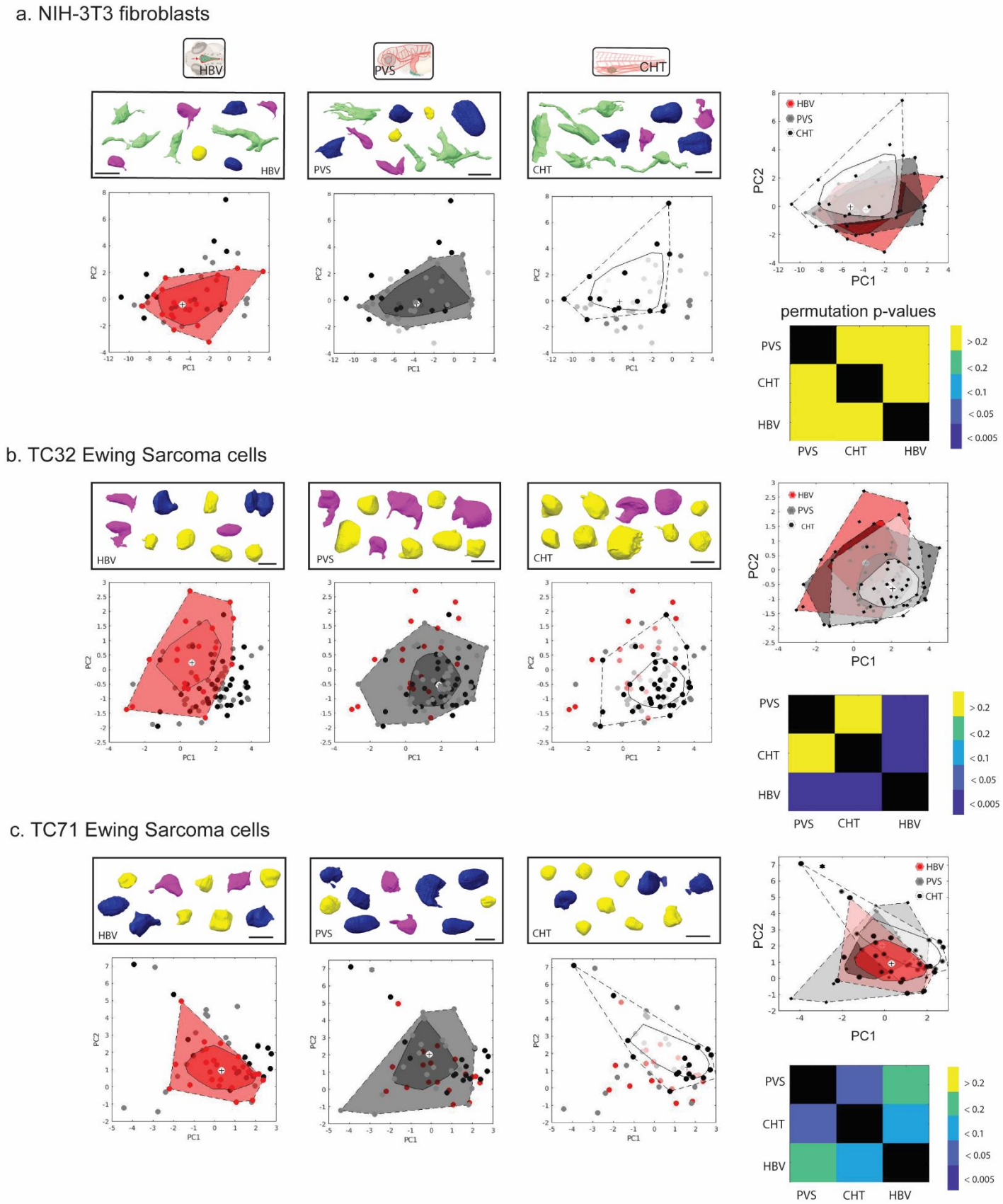

Figure 4: Tissue microenvironment affects EwS cell morphologies. (a-c) 10 representative cell renderings of EwS cell lines TC32 and TC71 and fibroblast cell line NIH-3T3 are shown, color-coded by k-means-based cluster from Figure 2e

(black frames, upper part of panels). Bagplots below display PCA of each cell line as a function of region (HBV-red, PVS, black, CHT, white). The inner polygon is constructed on the basis of Tukey depth, and contains at most 50% of the data points. The outer circle encompasses all data excluding outliers. White plus sign represents the Tukey depth median. Lower right panel shows a similarity matrix based on pairwise permutation tests. Note that relative to NIH-3T3 which shows high similarity in morphological cell state among all three regions (a), TC32 (b) and TC71 (c) show some tissue-dependent specialization of cells. Scale bars: 20 µm.

proportions of NN/PE/E cells within the CHT and HBV, but a

bias towards PE cells in the PVS (Figure S4d), which may be an experimental limitation of the imaging framework, as clusters in the PVS are significantly larger in size (Figure S2e). Taken together, these results demonstrate a sensitivity of EwS cell morphological state to both nascent tissue ME and contact-driven cues from neighboring cancer cells, demonstrating their potential for context-driven cell adaptation.

Loss of EWSR1-FLI1 causes variable changes in morphologies as a function of tissue microenvironment

Previous works have suggested that variation in EWSR1-FLI1 expression could drive differential cell function [43, 58]. Using our dox-inducible EF1 knockdown system, we observed efficient partial reduction in EF1 (Figure S5a) and EF1-dependent differences in cytoskeletal organization in 2D (Figure S5b). Notably, the change in cytoskeletal organization did not lead to striking cell shape changes in 2D in our assays. We did, however, observe marked shifts in cell morphology in the xenograft assays (Fig. 2). We next examined whether loss of EF1 affected the cell morphological states in a tissue-sensitive

manner. In our xenograft assay, TC32 control (C) shRNA showed distinct morphological states in HBV, PVS and CHT, with cells in PVS shifting to a relatively more protrusive state (left in PC1) and those in HBV shifting upward in PC2 and higher in volume ((Figure 6a-b, Figure S5c-d). Loss of EF1 caused larger heterogeneity in morphological cell state and a significant shift of cells in all three regions to a more protrusive state (Figure 6c-d, Figure S5c). Interestingly, differences in morphological state between PVS and CHT became relatively blurred in EF1 shRNA group, while HBV cells remained distinctly higher in PC2 and volume. Pseudorosette-like structures also formed in HBV with EF1 low cells, despite altered morphology (Figure 6e, Movie S2), suggesting maintained sensitivity to the environmental cues of this environment. Examination of sphericity as a function of position within a cluster in the C or EF1 shRNA expressing cells showed that cells with distinctly low sphericity could be observed with only partial contact with other cells upon EF1 knockdown (Figure 6f). This is in contrast to the requirement for high degree of contact with cells for the protrusive phenotype observed in TC32 and TC71 (Figure 5h, Figure S4c), suggesting differential sensitivity of response to surrounding cancer cells with decreased EF1 expression. We conclude that reduced EF1 expression leads to an indiscrimately more protrusive morphological cell state with loss of sensitivity to some but not all environmental cues.

In general, we demonstrated the ability of the presented framework to resolve environmentally-driven single-cell phenotypes *in situ*. Several technological innovations made this workflow possible. First, the improved axial resolution by ASLM compared to other light-sheet imaging modalities, including advanced techniques such as lattice light-sheet microscopy [59, 60], enabled high-resolution visualization of cells in 3D which would be otherwise impossible (Figure S5a). This is particularly important in cancer cell biology as opposed to tissue development, where orientation of cells is

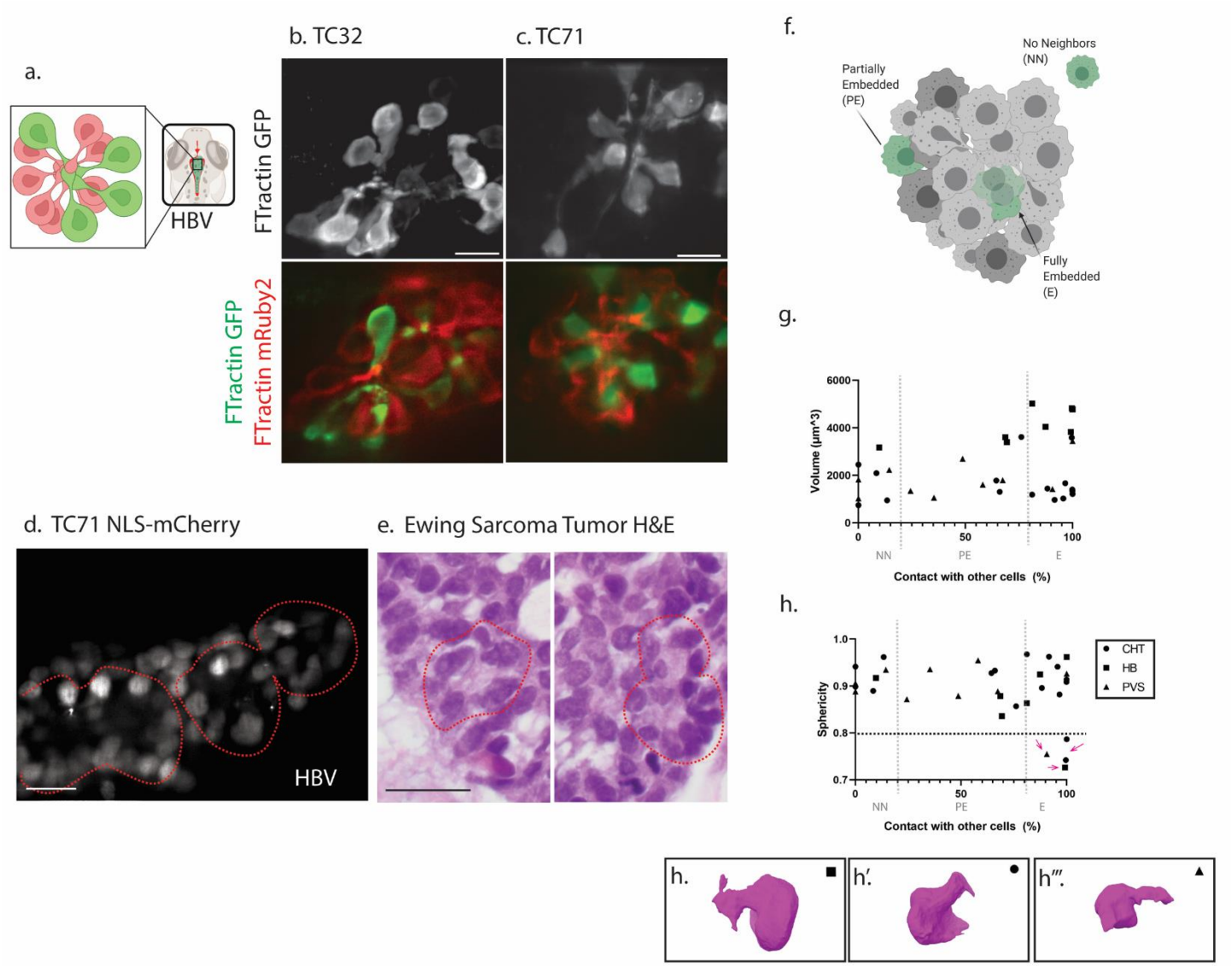

Figure 5: Tissue architecture affects cell state. (a) schematic of mixtures of flourescently labeled cells displaying pseudo-rosette-like formations formed by EwS cells specifically in hindbrain ventricles (HBVs). **(b-c)** Maximum intensity projections (upper panel) or single optical slices (lower panel) of TC32 and TC71 cells expressing Ftractin-GFP (grey, green) or F-Tractin-mRuby2 (red), in zebrafish larval hindbrain ventricle (3dpf). Note the pseudorosette-like polarization of cells, with cellular protrusions pointing towards a center of a sphere and cell bodies organized outwards. **(d)** Single optical slice of TC71 cells expressing nuclear marker H2B-Cherry form ring-like structures (outlined with dashed red line) in the HBV which resemble those observed in peripheral primitive neuroectodermal tumors ppNETs. **(e)** An H&E stained histological slice from a human Ewing Sarcoma tissue sample evaluated by a pathologist. Psuedorosettes structures outlined with dashed red line. **(f)** Cells within a cell cluster of like-cells are classified and analyzed according to percent contact with other cells, as *no neighbors* (NN, 0-20% contact with other cells), *partially exposed* (PE, 21%-81% contact), or fully *embedded* (E, 81-100% contact). **(g-h)** Proportion of contact with other TC32 cells is plotted against two dominant shape features, Volume (g) and Sphericity (h). While no clear relationship can be uncoupled from tissue ME for volume, a few embedded cells but not other groups show cells with distinctly low sphericity (>0.8, dashed line). Arrows indicate cells from all 3 regions with distinctive cell morphological states, rendered in h'-h''' and color-coded by k-means clustering in Figure 2e. Scale bars 20um.

disordered and random. Simulations reducing the axial resolution 3-fold yielded segmentation errors and marked shifts in PCA space, demonstrating the importance of high, near-isotropic resolution in 3D measurements (Figure S5b-c). Second, due to inherent cell-to-cell variation, this type of analysis is only

possible with examination of a fairly large dataset. For example, random removal of 50% of the data caused loss of sensitivity to differences between experimental groups (Figure S5d). Third, the automation of the single-cell segmentation and quantification, using constant cell surface extraction parameters, enabled high-throughput and unbiased analysis. These technical developments enabled the analysis of single cancer cell states within clusters of cancer cells within living tissues in the zebrafish, providing a powerful basis to study cancer cell adaptation.

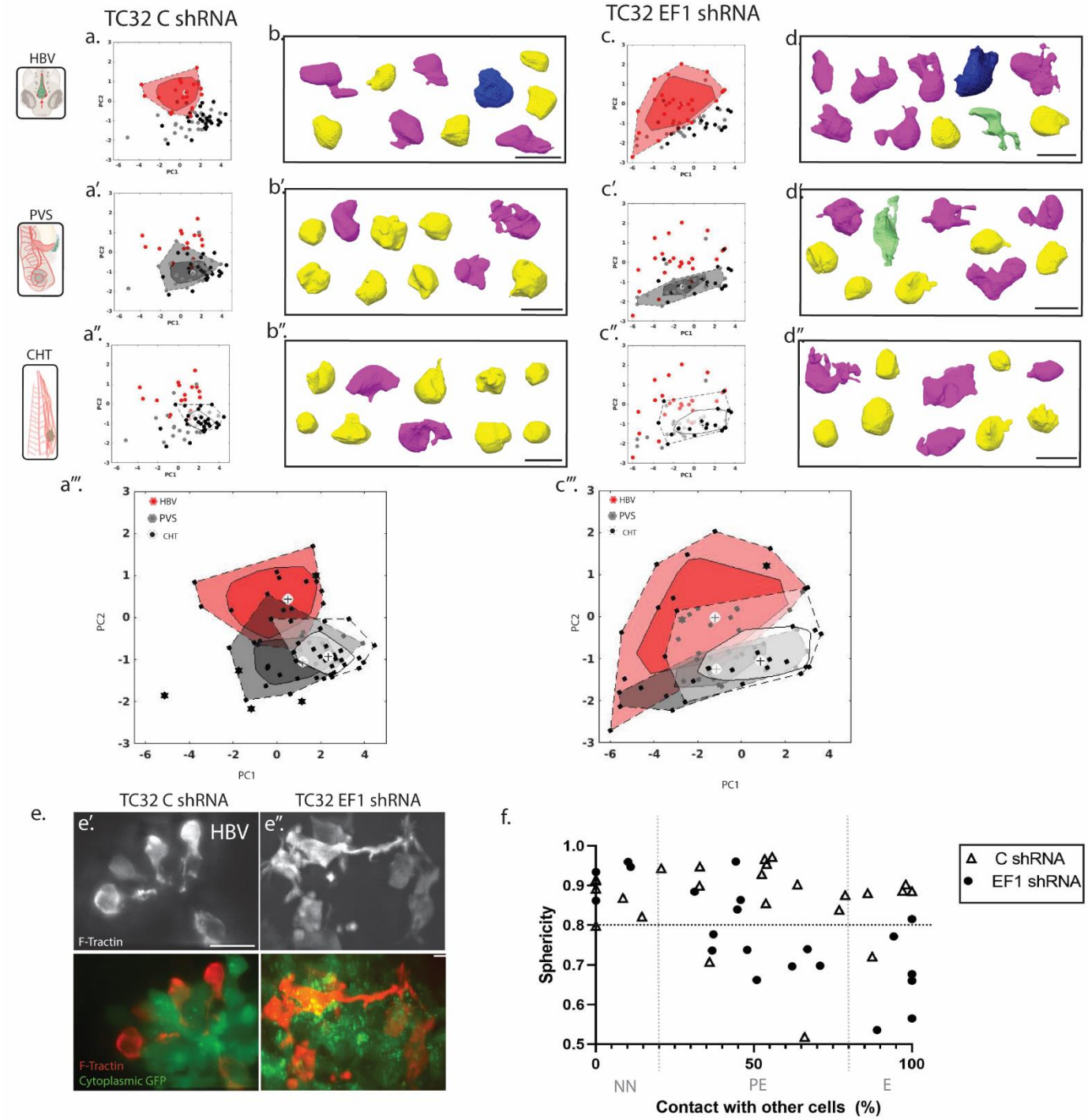

Figure 6: Knockdown of EF1 causes variable changes in morphologies as a function of tissue microenvironment. (a-d) Morphological cell states were examined as a function of tissue microenvironment in EwS cells expressing a dox-inducible scrambled (C) or EF1 targeting shRNA. In C shRNA expressing cells, all 3 regions show distinct cell states in PCA space (a-a‴, b-b″). Upon knockdown of EF1, cells are shifted to a more protrusive state and differences as a

function of region are relatively reduced (c-c''', d-d''). **(e)** A subset of EwS C (e') or EF1 (e'') shRNA expressing cells express F-Tractin mRuby2 (white in top panel, red in bottom panel) in addition to dox-inducible cytoplasmic GFP (green, bottom panel), allowing for labelling of individual cells. EwS cells in HBV can maintain a pseudorosette-like organization upon EF1 knockdown, despite altered cell morphologies. (see also movie S2). **(f)** Proportion of contact with other TC32 cells expressing C shRNA or EF1 shRNA is plotted against Sphericity. Under both experimental conditions cells with distinctly low sphericity (>.8, dashed line) appear predominantly in the *embedded* (E) cells, suggesting cues from neighboring cancer cells are required for this phenotype. Scale bar 20 µm.

Discussion

In this study, we present classification of Ewing Sarcoma (EwS) cell morphology in zebrafish xenografts as a tool to study cancer cell adaptation to diverse tissue microenvironments. We demonstrate a 3D imaging and machine-learning pipeline that captures heterogeneity of cell responses at the single cell level. Using this framework, we uncover systematic shifts in EwS cell morphological states as a function of cell type, oncogene expression level, and tissue microenvironment.

Demonstrating that cancer cells change in response to extrinsic mechanical or other cues during metastasis has been a difficult question to tackle, largely due to heterogeneity in cellular response. Our approach begins to address this challenge by leveraging the combined advantages of the zebrafish model [6-9] and recent innovations in light-sheet imaging [40, 42, 61], allowing for the throughput and resolution needed to uncover heterogeneous distributions of noisy data. Thus, we show that both nascent tissue ME and cancer-driven changes in ME affect EwS cell states (Figure 7). Interestingly, non-transformed fibroblasts, while highly heterogeneous in morphology, showed no relationship with tissue ME, suggesting that specialization for certain environments could be a particular feature associated with cell transformation.

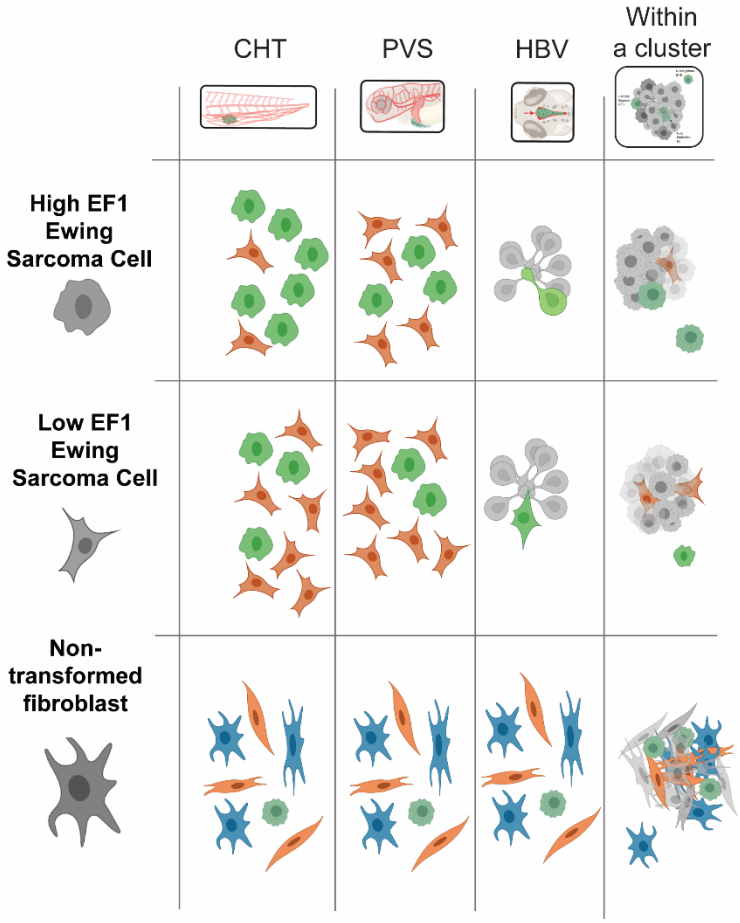

Figure 7: Ewing Sarcoma morphological cell state displays context-specific cellular adaptation. A schematic representing findings. High EF1 expressing EwS cells show a change in morphological state or organization according to seeding site or location within a cluster. Low expression of EF1 causes a shift towards more protrusive cell state and reduced sensitivity to some tissue environmental cues but not others, suggesting EF1 enables site-specific specialization of cancer cells. In contrast, non-transformed fibroblasts display highly heterogeneous cell morphologies regardless of

Our results also show that expression levels of EF1 can regulate morphological cell state, as reduced expression of EF1 leads to more protrusive cell morphologies. This is consistent with previously reported observations of EwS in cell culture *in vitro*, where reduced EF1 expression showed cell state shifts with transcriptional and morphological characteristics of epithelial-to-mesenchymal

transitions (EMT) [43] and decreased proliferation [62, 63]. It is notable that the reduction of EF1 expression causes more protrusive cell states in all three tissue MEs and displayed a relative loss of sensitivity to contact with other cancer cells, although rosette-like formations in the HBV remained.

Based on these results, we propose a model where EwS cells through high expression of EF1 maintain a “high-plasticity cell state” (HPCS) similar to that observed in lung cancer [64], which allows them to adapt to distinct tissue microenvironments during metastasis. Low expression of EF1 confers a loss of plasticity and reduced proliferation which are properties associated with a more differentiated cell state, and could potentially provide a survival advantage under variable cellular stresses. A more differentiated state may also be triggered by cell-extrinsic cues from neighboring tissues or cancer cells. Upon receipt of the relevant environmental cues or through stochastic cell behavior, the cell may revert to the HPCS state and resume outgrowth at a secondary metastatic site. This is complementary to existing models in the EwS field, which suggests that modulation of levels of EF1 can enable switch-like behavior from proliferative to migratory states [43, 58]. Future work will determine if tissue ME-dependent modulation of cell states works in parallel or in conjunction with regulation of EF1.

Limitations and future prospects

While this work represents a significant advancement in characterization of cell adaptation as a function of tissue microenvironments, several limitations of the current approach must be considered. First, while morphology serves as a powerful functional output for cell state, it is by nature a conglomerate of many mechanical [18, 65, 66], biochemical [13, 14], and cell-intrinsic [11, 67] cues and therefore cannot inform on the specific biochemical pathways regulating signaling. Therefore, correlating specific morphological states to organization of mechanical and biochemical signaling pathways at single-cell resolution will allow triangulation of cell states for a deeper understanding of tissue-dependent cell differences. Our pipeline already encompasses the microscopy resolution that is necessary for imaging and analysis of subcellular molecular behaviors. Further, the throughput of the assay, while an improvement from other techniques, could be greatly enhanced if mosaic labeling was expanded to multicolor techniques such as brainbow [68]. Also, while the zebrafish embryonic xenograft model confers many advantages, it is limited to the short timescale of 2-10 days post-engraftment. To investigate longer term cell adaptations, complementary similar approaches could be applied to adult immunocompromised zebrafish [69], organoid [70, 71], and murine cancer models [72] as technological limitations allow. Future work will also leverage the potential in this system for studying dynamics of cell behavior through live imaging and broader application to other cancer models.

Together this work presents a new framework to study cancer cell adaptation to diverse microenvironmental cues at single-cell resolution, and sheds light on the ability of EwS cells to specialize by integrating cell-intrinsic and cell-extrinsic cues.

Methods:

Zebrafish husbandry

Danio rerio were maintained in an Aquaneering aquatics facility according to industry standards. Vertebrate animal work was carried out by protocols approved by the institutional animal care and use committee, at UT Southwestern, an AAALAC accredited institution. WIK wild-type lines used were obtained from the Zebrafish International Resource Center (zebrafish.org).

Cell culture and cell line generation

Cells were cultured at 5% CO2 and 21% O2. TC32 (a gift from R. Deberardinis, UTSW) and TC71 cells (a gift from A. Whitehurst, UTSW) were cultured using RPMI (Gibco) supplemented with 10% fetal bovine serum and 1% antibiotic antimycotic. NIH-3T3 cells (a gift from Schmid lab, UTSW) were cultured using DMEM (Gibco) supplemented with 10% fetal bovine serum and 1% antibiotic antimycotic. TC32 shRNA lines (a gift from D. McFadden, UTSW) cells were generated using the pZIP shRNA Promoter selection kit (transomics.com). EF1 shRNA targets the C-terminal region of Fli1 and the C shRNA is a scrambled sequence. shRNA cells were cultured using RPMI (Gibco) supplemented with 10% fetal bovine serum and 1% antibiotic antimycotic. shRNA knockdown was verified by western blotting using rabbit anti-Fli1 (AbCam ab15289) (Figure S3).

Flourescent constructs were introduced into cells using the pLVX lentiviral system (Clontech) and selected using antibiotic resistance to either puromycin or neomycin. The GFP-FTractin and mRuby2-FTractin constructs contain residues 9–52 of the enzyme IPTKA30 fused to eGFP or mRuby2, respectively. pLenti6-H2B-mCherry was a gift from Torsten Wittmann (Addgene plasmid #89766) [73].

Xenografts

For xenografts of NIH-3T3, TC71, and TC32, preparation of cell mixture consisted of 99% or 90% mRuby2-Ftractin labeled cells and 1% or 10% GFP-FTractin labeled cells, for HBV and PVS, or CHT, respectively. These ratios were chosen to achieve optimum number of isolated cells not contacting other cells within a cluster. Cell mixture ($2x10^6$ cells) were run through a 70um cell strainer and resuspended in 5% FBS mixture for optimal cell viability.

Zebrafish embryos were collected, dechorionated and treated with 0.1 mM phenylthiourea (PTU) at 24 hpf to prevent pigmentation. Fish xenografts consisted of microinjection of cell mixture into zebrafish larvae (2 dpf) with glass capillary needles into PVS or HBV. For each cell xenograft group, cells are injected into 3-aminobenzoic acid ethyl ester (Tricaine) anesthetized embryos. For PVS injections, larvae with cells disseminated to the CHT through passive pressure via the vasculature during injection were selected for under a fluorescent stereomicroscope 1 hour post injections, to (1) increase the throughput of imaging by having two seeding sites within one embryo and (2) to select specifically for seeding-site specific cell adaptation rather than selection of a potentially more migratory population from the primary site of injection. Injected zebrafish larvae were incubated for 1-2 days in 34 ℃ before imaging.

Immunofluorescence:

For immunostaining of zebrafish larvae, anesthetized embryos were fixed in 4% paraformaldehyde/1XPBS for 2hrs in scintillation vials, rinsed in PBS +0.5% TritonX (PBST), and stored in PBS up to two weeks. Immunostaining was carried out as previously described [74]. Primary antibodies were rabbit anti-GFP (AbCam, ab290) and mouse anti-Phospho-Histone H3 (Cell Signaling, 9706S). TUNEL assay was performed using the ApopTag Green In-Situ Apoptosis Detection Kit (Millipore). Xenografted fish were immunostained for GFP prior to high resolution imaging of single cells.

Human Tumor Histology

Ewing Sarcoma tissue samples were obtained as part of standard clinical management. All histology samples were evaluated by an expert sarcoma pathologist.

Imaging

Light-sheet fluorescence microscopes were used to image the zebrafish larvae. Fixed zebrafish larvae were embedded in 1% low-melting agarose into sonicated, ethanol-washed Fluorinated Ethylene propylene (FEP) tubes (Zeus, HS 029EXP/ .018 REC). The tube is held by a custom-made mount, which allows 3D translation and rotation in our light-sheet microscopes.

For high-resolution 3D imaging of cell morphologies, axially swept light-sheet microscopy (ASLM) was developed as previously described [40, 75]. Briefly, a 25X, NA1.1 objective water-dipping (CFI75 Apo 25XC W, Nikon Instruments) is used for detection, in combination with a 500 mm achromatic convex lens (49-396, Edmund Optics), which forms the image with a total magnification of 62.5X on an sCMOS camera (ORCA-Flash4.0, Hamamatsu Photonics). A 28.6X NA0.7 water-dipping objective (54-10-7@488-910nm, Special Optics) is used for light-sheet illumination. In our ASLM set-up, the resolution is approximately 300 nm laterally and 450 nm axially over a 200x100 μm^2 field of view (FOV).

For imaging of immunostained fish larvae, a conventional multidirectional selective plane imaging microscope (mSPIM) [76] is used as previously described [77]. Briefly, a 16X NA 0.8 water-dipping objective (CFI75 LWD 16XW, Nikon Instruments) is used for detection. In combination with a 200 mm tube lens (58-520, Edmund Optics) forms the image on an sCMOS camera (ORCA-Flash4.0, Hamamatsu Photonics). The lateral resolution is approximately 350-400 nm. A 10X NA 0.28 objective (M Plan Apo 10x, 378-803-3, Mitutoyo) is used for light-sheet illumination. The thickness and the length of the light-sheet are controlled by a variable slit (VA100C, Thorlabs) placed at the conjugate plane of the back focal plane of the illumination objective. Usually, we adjust the variable slit to create a light-sheet with a thickness of 3-4 µm, which has a length of approximately 400 µm to cover a large FOV. Under these conditions, the axial resolution is estimated at 1.4 µm.

Image Processing

For high resolution 3D morphology imaging, regions of interest around individual cells were detected automatically by thresholding the smoothed image (sigma=5, thresholded at 5%) and computing the connected components, and subsequently isolating the corresponding raw data image. In some cases, additional user-aided cropping is done using ImageJ. We then applied drift correction using StackReg plugin [78] in ImageJ [79] to counter sample movement in Z during acquisition, via MIJ, a java package for running ImageJ within MATLAB. Finally, we applied deconvolution to all images prior to segmentation, using blind deconvolution with an experimentally acquired PSF with 10 iterations in MATLAB.

Segmentation and Geometric feature extraction

For 3D morphology classification, we employed a 3D morphology pipeline developed by Driscoll *et* al. [12] to create binary images of deconvoluted cell images. For the segmentation process, we smoothed the deconvoluted images with a 3D Gaussian kernel ($\sigma = 3$ pixels) and applied a gamma correction ($\Upsilon = 0.7$), then employed an Otsu threshold, followed by a 3D grayscale flood-fill operation to fill the potential holes. Disconnected parts from the main image were removed. The binary images were created based on the Otsu grayscale level and used for the shape descriptors analysis. All cells were manually examined for segmentation artifacts.

Computation 3D shape descriptors require parameters including volume, surface area, 3D convex hull, minimum circumscribed sphere and maximum inscribed sphere. The basic shape descriptors are calculated using 'regionprops3' in MATLAB for 3D segmented cells. Other features are calculated based on the formulas described (Table S1). These features include but are not limited to roughness, various definitions of sphericity, and 3D aspect ratio.

For location within clusters, the region of interests detectors described above was reused to isolate segmented volumes. Individual cell surfaces were extracted from cell volumes using *Surfaces maps* from 3D Object Counter plugin in Fiji [80]. Measurements of percent of contact with other cells were made based on measurements of colocalization of the surfaces of the subsequent binary images. These were compared to individual geometric features as captured by the 3D morphology pipeline described above.

For quantification of proliferation and apoptosis within clusters, we utilized manually-aided threshold based segmentation followed by 3D Objects Counter plugin [80] in ImageJ. Size of cluster or touching objects was estimated by dividing measured volume of the object with measured volume of an isolated object (e.g. PH3-labeled nucleus) within the same fish.

For quantification of change in cluster size over three days (Figure S2a-d), segmentation of areas of interest and measurements of changes in area were done in Cell Profiler [81].

Statistics and Visualizations

Violin plots, boxplots, and scatter plots of individual features at the cell-level or fish-level and corresponding statistical tests were performed using GraphPad Prism 9 (La Jolla, Ca). Outliers for individual parameters were found by ROUT method (Q = 1%) and excluded from analysis. To address sample variability, fish level data points were generated based on median of each geometrical feature per fish per region. Sample sizes are provided in figure legends.

For multivariable statistical analysis, Principal Component Analysis (PCA), scatter plots of PCs, and biplot were applied or generated in MATLAB. For visualization purpose, we defined the geometrical classes using the unsupervised learning k-means clustering algorithm in 2D PCA space and calculated the contribution of each geometrical classes in each experimental condition by hierarchical clustering. Bagplots were generated in MATLAB as described in *Verboven and Hubert,* 2010 [51, 82, 83].

Similarity matrices were based on pairwise permutation p-values between different conditions. The metric used for permutation test (n=1500 iterations) was the Tukey median of each distribution, as defined by [51].

3D surface renderings of single cells were created with ChimeraX [84] as described in *Driscoll et al*. [12]. Rendering of microscopy set-up was created with AutoCad (Autodesk). 3D rendering in Figure S2 created with Amira software (ThermoFisher). Schematics were created with BioRender.com.

Acknowledgments

We would like to think Meghan Driscoll, Erik Welf, and Marcel Mettlen for fruitful discussion and help with image analysis. Funding for this work in the Danuser lab has been provided through grants R35 GM136428 (NIH) and RP160157 (CPRIT). Dagan Segal holds an EMBO Long-term Research Fellowship (ALTF 626-2018).

1. Lambert, A.W., D.R. Pattabiraman, and R.A. Weinberg, *Emerging Biological Principles of Metastasis.* Cell, 2017. **168**(4): p. 670-691.
2. Bacac, M. and I. Stamenkovic, *Metastatic cancer cell.* Annu Rev Pathol, 2008. **3**: p. 221-47.
3. Gomez-Cuadrado, L., et al., *Mouse models of metastasis: progress and prospects.* Dis Model Mech, 2017. **10**(9): p. 1061-1074.
4. Katt, M.E., et al., *In Vitro Tumor Models: Advantages, Disadvantages, Variables, and Selecting the Right Platform.* Front Bioeng Biotechnol, 2016. **4**: p. 12.
5. van Marion, D.M., et al., *Studying cancer metastasis: Existing models, challenges and future perspectives.* Crit Rev Oncol Hematol, 2016. **97**: p. 107-17.
6. Osmani, N. and J.G. Goetz, *Multiscale Imaging of Metastasis in Zebrafish.* Trends Cancer, 2019. **5**(12): p. 766-778.
7. Konantz, M., et al., *Zebrafish xenografts as a tool for in vivo studies on human cancer.* Ann N Y Acad Sci, 2012. **1266**: p. 124-37.
8. Heilmann, S., et al., *A Quantitative System for Studying Metastasis Using Transparent Zebrafish.* Cancer Res, 2015. **75**(20): p. 4272-4282.
9. Ingham, P.W., *The power of the zebrafish for disease analysis.* Hum Mol Genet, 2009. **18**(R1): p. R107-12.
10. Calizo, R.C., et al., *Cell shape regulates subcellular organelle location to control early Ca(2+) signal dynamics in vascular smooth muscle cells.* Sci Rep, 2020. **10**(1): p. 17866.
11. Keren, K., et al., *Mechanism of shape determination in motile cells.* Nature, 2008. **453**(7194): p. 475-80.
12. Driscoll, M.K., et al., *Robust and automated detection of subcellular morphological motifs in 3D microscopy images.* Nat Methods, 2019. **16**(10): p. 1037-1044.
13. Yin, Z., et al., *A screen for morphological complexity identifies regulators of switch-like transitions between discrete cell shapes.* Nat Cell Biol, 2013. **15**(7): p. 860-71.
14. Bakal, C., et al., *Quantitative morphological signatures define local signaling networks regulating cell morphology.* Science, 2007. **316**(5832): p. 1753-6.
15. Sailem, H.Z. and C. Bakal, *Identification of clinically predictive metagenes that encode components of a network coupling cell shape to transcription by image-omics.* Genome Res, 2017. **27**(2): p. 196-207.
16. Lamouille, S., J. Xu, and R. Derynck, *Molecular mechanisms of epithelial-mesenchymal transition.* Nat Rev Mol Cell Biol, 2014. **15**(3): p. 178-96.
17. Woods, E.C., et al., *A bulky glycocalyx fosters metastasis formation by promoting G1 cell cycle progression.* Elife, 2017. **6**.
18. Kai, F., H. Laklai, and V.M. Weaver, *Force Matters: Biomechanical Regulation of Cell Invasion and Migration in Disease.* Trends Cell Biol, 2016. **26**(7): p. 486-497.

19. Wu, P.H., et al., *Evolution of cellular morpho-phenotypes in cancer metastasis.* Sci Rep, 2015. **5**: p. 18437.
20. Thakar, R.G., et al., *Cell-shape regulation of smooth muscle cell proliferation.* Biophys J, 2009. **96**(8): p. 3423-32.
21. Mills, J.C., et al., *Apoptotic membrane blebbing is regulated by myosin light chain phosphorylation.* J Cell Biol, 1998. **140**(3): p. 627-36.
22. Chen, C.S., et al., *Geometric control of cell life and death.* Science, 1997. **276**(5317): p. 1425-8.
23. Rohban, M.H., et al., *Systematic morphological profiling of human gene and allele function via Cell Painting.* Elife, 2017. **6**.
24. Wu, P.H., et al., *Single-cell morphology encodes metastatic potential.* Sci Adv, 2020. **6**(4): p. eaaw6938.
25. Zaritsky, A., et al., *Interpretable deep learning of label-free live cell images uncovers functional hallmarks of highly-metastatic melanoma.* bioRxiv, 2020: p. 2020.05.15.096628.
26. Derynck, R. and R.A. Weinberg, *EMT and Cancer: More Than Meets the Eye.* Dev Cell, 2019. **49**(3): p. 313-316.
27. Bera, K., et al., *Artificial intelligence in digital pathology - new tools for diagnosis and precision oncology.* Nat Rev Clin Oncol, 2019. **16**(11): p. 703-715.
28. McGranahan, N. and C. Swanton, *Clonal Heterogeneity and Tumor Evolution: Past, Present, and the Future.* Cell, 2017. **168**(4): p. 613-628.
29. Crompton, B.D., et al., *The genomic landscape of pediatric Ewing sarcoma.* Cancer Discov, 2014. **4**(11): p. 1326-41.
30. Grobner, S.N., et al., *The landscape of genomic alterations across childhood cancers.* Nature, 2018. **555**(7696): p. 321-327.
31. Grunewald, T.G.P., et al., *Ewing sarcoma.* Nat Rev Dis Primers, 2018. **4**(1): p. 5.
32. Delattre, O., et al., *The Ewing family of tumors--a subgroup of small-round-cell tumors defined by specific chimeric transcripts.* N Engl J Med, 1994. **331**(5): p. 294-9.
33. Hernandez Tejada, F.N., et al., *Advances in the Management of Pediatric Sarcomas.* Curr Oncol Rep, 2020. **23**(1): p. 3.
34. Cotterill, S.J., et al., *Prognostic factors in Ewing's tumor of bone: analysis of 975 patients from the European Intergroup Cooperative Ewing's Sarcoma Study Group.* J Clin Oncol, 2000. **18**(17): p. 3108-14.
35. Miser, J.S., et al., *Treatment of metastatic Ewing's sarcoma or primitive neuroectodermal tumor of bone: evaluation of combination ifosfamide and etoposide--a Children's Cancer Group and Pediatric Oncology Group study.* J Clin Oncol, 2004. **22**(14): p. 2873-6.
36. Ladenstein, R., et al., *Primary disseminated multifocal Ewing sarcoma: results of the Euro-EWING 99 trial.* J Clin Oncol, 2010. **28**(20): p. 3284-91.
37. Ye, C., M. Dai, and B. Zhang, *Risk Factors for Metastasis at Initial Diagnosis With Ewing Sarcoma.* Front Oncol, 2019. **9**: p. 1043.
38. Kager, L., et al., *Primary metastatic osteosarcoma: presentation and outcome of patients treated on neoadjuvant Cooperative Osteosarcoma Study Group protocols.* J Clin Oncol, 2003. **21**(10): p. 2011-8.
39. Merks, J.H., et al., *Parameningeal rhabdomyosarcoma in pediatric age: results of a pooled analysis from North American and European cooperative groups.* Ann Oncol, 2014. **25**(1): p. 231-6.
40. Dean, K.M., et al., *Diagonally Scanned Light-Sheet Microscopy for Fast Volumetric Imaging of Adherent Cells.* Biophys J, 2016. **110**(6): p. 1456-65.
41. Dean, K.M., et al., *Deconvolution-free Subcellular Imaging with Axially Swept Light Sheet Microscopy.* Biophys J, 2015. **108**(12): p. 2807-15.
42. Reynaud, E.G., et al., *Guide to light-sheet microscopy for adventurous biologists.* Nat Methods, 2015. **12**(1): p. 30-4.

43. Franzetti, G.A., et al., *Cell-to-cell heterogeneity of EWSR1-FLI1 activity determines proliferation/migration choices in Ewing sarcoma cells.* Oncogene, 2017. **36**(25): p. 3505-3514.
44. Lowery, L.A. and H. Sive, *Initial formation of zebrafish brain ventricles occurs independently of circulation and requires the nagie oko and snakehead/atp1a1a.1 gene products.* Development, 2005. **132**(9): p. 2057-67.
45. Chang, J.T., M.K. Lehtinen, and H. Sive, *Zebrafish cerebrospinal fluid mediates cell survival through a retinoid signaling pathway.* Dev Neurobiol, 2016. **76**(1): p. 75-92.
46. Fame, R.M., et al., *Directional cerebrospinal fluid movement between brain ventricles in larval zebrafish.* Fluids Barriers CNS, 2016. **13**(1): p. 11.
47. Nicoli, S. and M. Presta, *The zebrafish/tumor xenograft angiogenesis assay.* Nat Protoc, 2007. **2**(11): p. 2918-23.
48. Murayama, E., et al., *Tracing hematopoietic precursor migration to successive hematopoietic organs during zebrafish development.* Immunity, 2006. **25**(6): p. 963-75.
49. Tamplin, O.J., et al., *Hematopoietic stem cell arrival triggers dynamic remodeling of the perivascular niche.* Cell, 2015. **160**(1-2): p. 241-52.
50. Xue, Y., et al., *The Vascular Niche Regulates Hematopoietic Stem and Progenitor Cell Lodgment and Expansion via klf6a-ccl25b.* Dev Cell, 2017. **42**(4): p. 349-362 e4.
51. Rousseeuw, P.J., Ruts Ida, Tukey, John W. , *The Bagplot: A Bivariate Boxplot.* The American Statistician, 1999. **53**(4).
52. Llombart-Bosch, A., et al., *Histological heterogeneity of Ewing's sarcoma/PNET: an immunohistochemical analysis of 415 genetically confirmed cases with clinical support.* Virchows Arch, 2009. **455**(5): p. 397-411.
53. Brohl, A.S., et al., *The genomic landscape of the Ewing Sarcoma family of tumors reveals recurrent STAG2 mutation.* PLoS Genet, 2014. **10**(7): p. e1004475.
54. Campbell, K., et al., *Comparison of Epidemiology, Clinical Features, and Outcomes of Patients with Reported Ewing Sarcoma and PNET over 40 Years Justifies Current WHO Classification and Treatment Approaches.* Sarcoma, 2018. **2018**: p. 1712964.
55. Navarro, S., et al., *Immunophenotypic profile of biomarkers related to anti-apoptotic and neural development pathways in the Ewing's family of tumors (EFT) and their therapeutic implications.* Anticancer Res, 2007. **27**(4B): p. 2457-63.
56. Snijder, B., et al., *Population context determines cell-to-cell variability in endocytosis and virus infection.* Nature, 2009. **461**(7263): p. 520-3.
57. Mayr, U., D. Serra, and P. Liberali, *Exploring single cells in space and time during tissue development, homeostasis and regeneration.* Development, 2019. **146**(12).
58. Aynaud, M.M., et al., *Transcriptional Programs Define Intratumoral Heterogeneity of Ewing Sarcoma at Single-Cell Resolution.* Cell Rep, 2020. **30**(6): p. 1767-1779 e6.
59. Chen, B.C., et al., *Lattice light-sheet microscopy: imaging molecules to embryos at high spatiotemporal resolution.* Science, 2014. **346**(6208): p. 1257998.
60. Chang, B.J., K.M. Dean, and R. Fiolka, *Systematic and quantitative comparison of lattice and Gaussian light-sheets.* Opt Express, 2020. **28**(18): p. 27052-27077.
61. Welf, E.S., et al., *Quantitative Multiscale Cell Imaging in Controlled 3D Microenvironments.* Dev Cell, 2016. **36**(4): p. 462-75.
62. Toomey, E.C., J.D. Schiffman, and S.L. Lessnick, *Recent advances in the molecular pathogenesis of Ewing's sarcoma.* Oncogene, 2010. **29**(32): p. 4504-16.
63. Hancock, J.D. and S.L. Lessnick, *A transcriptional profiling meta-analysis reveals a core EWS-FLI gene expression signature.* Cell Cycle, 2008. **7**(2): p. 250-6.
64. Marjanovic, N.D., et al., *Emergence of a High-Plasticity Cell State during Lung Cancer Evolution.* Cancer Cell, 2020. **38**(2): p. 229-246 e13.

65. Baskaran, J.P., et al., *Cell shape, and not 2D migration, predicts extracellular matrix-driven 3D cell invasion in breast cancer.* APL Bioeng, 2020. **4**(2): p. 026105.
66. Park, J.S., et al., *Mechanical regulation of glycolysis via cytoskeleton architecture.* Nature, 2020. **578**(7796): p. 621-626.
67. Alizadeh, E., et al., *Cellular morphological features are predictive markers of cancer cell state.* Comput Biol Med, 2020. **126**: p. 104044.
68. Livet, J., et al., *Transgenic strategies for combinatorial expression of fluorescent proteins in the nervous system.* Nature, 2007. **450**(7166): p. 56-62.
69. Yan, C., et al., *Visualizing Engrafted Human Cancer and Therapy Responses in Immunodeficient Zebrafish.* Cell, 2019. **177**(7): p. 1903-1914 e14.
70. Hartley, B.J. and K.J. Brennand, *Neural organoids for disease phenotyping, drug screening and developmental biology studies.* Neurochem Int, 2017. **106**: p. 85-93.
71. Drost, J. and H. Clevers, *Organoids in cancer research.* Nat Rev Cancer, 2018. **18**(7): p. 407-418.
72. Lamprecht, S., et al., *Multicolor lineage tracing reveals clonal architecture and dynamics in colon cancer.* Nat Commun, 2017. **8**(1): p. 1406.
73. Pemble, H., et al., *GSK3-mediated CLASP2 phosphorylation modulates kinetochore dynamics.* J Cell Sci, 2017. **130**(8): p. 1404-1412.
74. Miller, A.C., et al., *Neurobeachin is required postsynaptically for electrical and chemical synapse formation.* Curr Biol, 2015. **25**(1): p. 16-28.
75. Isogai, T., et al., *Direct Arp2/3-vinculin binding is essential for cell spreading, but only on compliant substrates and in 3D.* bioRxiv, 2019: p. 756718.
76. Huisken, J. and D.Y. Stainier, *Even fluorescence excitation by multidirectional selective plane illumination microscopy (mSPIM).* Opt Lett, 2007. **32**(17): p. 2608-10.
77. Murali, V.S., et al., *An image-based assay to quantify changes in proliferation and viability upon drug treatment in 3D microenvironments.* BMC Cancer, 2019. **19**(1): p. 502.
78. Thevenaz, P., U.E. Ruttimann, and M. Unser, *A pyramid approach to subpixel registration based on intensity.* IEEE Trans Image Process, 1998. **7**(1): p. 27-41.
79. Schindelin, J., et al., *Fiji: an open-source platform for biological-image analysis.* Nat Methods, 2012. **9**(7): p. 676-82.
80. Bolte, S. and F.P. Cordelieres, *A guided tour into subcellular colocalization analysis in light microscopy.* J Microsc, 2006. **224**(Pt 3): p. 213-32.
81. McQuin, C., et al., *CellProfiler 3.0: Next-generation image processing for biology.* PLoS Biol, 2018. **16**(7): p. e2005970.
82. Verboven, S., Hubert, Mia, *Matlab library LIBRA.* Wiley Interdisciplinary Reviews: Computational Statistics, 2010(2): p. 509-515.
83. Hubert, M., Van der Veeken, Stephan, *Outlier detection for skewed data.* Journal of Chemometrics, 2008. **22**: p. 235-246.
84. Goddard, T.D., et al., *UCSF ChimeraX: Meeting modern challenges in visualization and analysis.* Protein Sci, 2018. **27**(1): p. 14-25.